Accepted Manuscript

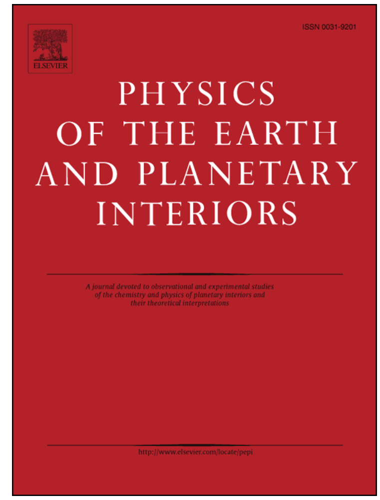

Brittle-ductile transition depth versus convergence rate in shallow crustal thrust faults: considerations on seismogenic volume and impact on seismicity

Patrizio Petricca, Eugenio Carminati, Carlo Doglioni, Federica Riguzzi

PII: S0031-9201(18)30055-4
DOI: https://doi.org/10.1016/j.pepi.2018.09.002
Reference: PEPI 6191

To appear in: *Physics of the Earth and Planetary Interiors*

Please cite this article as: Petricca, P., Carminati, E., Doglioni, C., Riguzzi, F., Brittle-ductile transition depth versus convergence rate in shallow crustal thrust faults: considerations on seismogenic volume and impact on seismicity, *Physics of the Earth and Planetary Interiors* (2018), doi: https://doi.org/10.1016/j.pepi.2018.09.002

Brittle-ductile transition depth versus convergence rate in shallow crustal thrust faults: considerations on seismogenic volume and impact on seismicity

Patrizio Petricca[a], Eugenio Carminati[a,b], Carlo Doglioni[a,c], Federica Riguzzi[c]

[a]*Dipartimento di Scienze della Terra, Universitá La Sapienza, Roma, Italy*
[b]*Istituto di Geologia Ambientale e Geoingegneria, CNR, Roma, Italy*
[c]*Istituto Nazionale di Geofisica e Vulcanologia, Roma, Italy*

Abstract

Earthquakes occur in the Earth's crust where rocks are brittle, with magnitude increasing with the volume involved in the coseismic stage. Largest volumes are expected in convergent tectonic settings since thrust fault may be even more than 25 times larger than hypocenter depth. In general, the maximum depth of hypocenters within the crust corresponds to the brittle-ductile transition (BDT). The deepening of the BDT increases the potential seismic volume, hence raising the energy released during an earthquake. Here, by means of 2-D thermo-mechanical modelling dedicated to intraplate thrusts and thrusts within fold-and-thrust belts (shallow crust), the deepening of the BDT depth in convergent settings with variable convergence rates is investigated. Results of models characterized by shallow faults (15°- 20° dip) show that BDT depth deepens by 15 km increasing the convergence rate from 1 to 10 cm/yr. Steeper thrust faults (25°- 40° dip) show a lower

Email address: patrizio.petricca@uniroma1.it (Patrizio Petricca)

degree of deepening of the BDT ($\simeq$ 5 km) as convergence rate is increased. Calculated BDT depths allow the calculation of maximum seismic volumes involved during thrust earthquakes. Deeper BDT depths obtained assuming higher convergence rates imply larger seismic volumes and an increase of 2 orders of magnitude of the stored potential energy, as effectively observed in nature.

Keywords: Thrust fault earthquakes, Continental crust, Seismic volume, Brittle-ductile transition depth, Convergence rate

1. Introduction

Compressional earthquakes mainly occur at convergent plate boundaries where the highest magnitudes and most shallow earthquakes have been recorded (Figure .1a). Released seismic energy scales with fault dimension [e.g., 1, 2, 3, 4] - and therefore with the rock volume involved during the coseismic stage [5, 6, 7, 8] - and with convergence rate [9, 10, 11].

The seismogenic volume is constrained by the fault length and the depth of the brittle-ductile transition (BDT) or the depth of the decollement layer [12]. Bird and Kagan (2004) [13] found that plate boundaries are associated with earthquakes characterized by seismic moment resulting from different thicknesses of coupled seismogenic lithosphere. The distribution of earthquake hypocenters gives a first approximation of the seismogenic thickness, and hence of the maximum depth of faulting [14]. For earthquakes with magnitude Mw>5 worldwide [15], earthquakes foci deepen where the largest events have been recorded (Mw>8.5), ranging in depth from 25 to 50 km and almost coinciding with convergent plate boundaries regions (e.g., Sumatra, Japan, Chile). Shallower hypocentral depths (<25 km) typify divergent and strike-slip margins where rarely Mw>8. Furthermore, thrust faults display higher ratios between fault length and hypocenter depth (up to more than 25) with respect to strike-slip and normal faults (around 10 and 3 respectively). This implies that thrusts are associated with the largest volumes activated at the coseismic stage [5].

A distinction may be made between shallow crustal and subduction-interface thrust earthquakes that differ in terms of tectonic loading mechanisms [e.g., 16]. Interplate ruptures at subduction interfaces [17], that release the largest part of seismic moment in convergent margins, evolve following a peculiar deformation cycle [18, 19] and respond to peculiar scaling laws relating magnitude and geometric/kinematics parameters [e.g., 20, 21]. Intraplate thrusts and thrusts within fold-and-thrust belts (shallow crustal) deliver a significant 20 to 30 % of the seismic energy budget and more evidently depend on the convergence rate [22].

While rupture-scaling relationships are routinely used in seismic hazard studies, (non)linear relations between relative plate velocity and seismicity rate or moment rate or maximum possible magnitude are harshly debated and considered true [11, 23, 24, 9, 10] or not [25, 26, 27] depending on assumptions and data selection [e.g., 28, 29]. Uncertainties derive also from the short period of global instrumental observations [10, 26, 30].

The lower boundary of the seismogenic layer reaches maximum depths of about 40 km [31, 32]. A comparison of convergence rates from GPS data (see Appendix A) with seismogenic depths extrapolated from available regional studies indicates that the faster the convergence, the thicker this seismogenic layer (Figure .1b and Table 1). For convergent plate margins, minimum seismogenic layer thicknesses (10-15 km) occur in slowly (0-2 cm/yr) convergent realms (Calabrian Arc [33, 34, 35], Apennines [14], Aegean and Zagros [36, 37]). Such thickness values increase to around 20 km in intermediate (4-6 cm/yr, i.e. India [37]) convergent settings. Although the focus of this work is not on megathrusts in subduction zones, the increase of seismogenic layer thickness with convergence rate applies also to these realms, as shown in figure .1 by the behavior of subduction zones characterized by intermediate (5-7 cm/yr, i.e. Cascadia [38, 39], Sumatra[39, 40, 41] and Chile [42]) and fast (up to 10 cm/yr, i.e. Japan [39, 43]) convergence.

Here, the relationship between convergence rate and BDT deepening is investigated by 2D thermo-mechanical models of shallow crustal thrust faults. Searching for the BDT depth values and considering homogeneous lithologies, the brittle-ductile behavior of rocks is evaluated depending on applied convergence rate in compressional tectonic regimes. In addition to the control provided by convergence rate, the effects of other parameters, i.e. the thermal structure of the domain [e.g., 44], and the viscous limit on strength [e.g., 45] are tested as well. Modelling results are used to calculate the available seismic volumes and predict the potential stored energy that may be released during an earthquake.

2. Modelling strategy

Implementing models to predict the location of the BDT for increasing/decreasing convergence rate is not a straightforward task. In fact, the BDT depth is not constant since it depends on a number of factors, including geothermal gradient (i.e., temperature), strain rate, stress regime, pore-fluid pressure and grain size [46, 47, 48, 49]. Rock strength profiles show that at relatively low temperatures and pressures (depth lower than 10-20 km) the crust is brittle. Strength of rocks linearly increases with depth under the control of the stress regime and fluid pressure [50, 51]. The buildup of deviatoric stress creates the condition to trigger earthquakes that occur once friction is overcome. For a rock of given mineralogical composition and rheological parameters, increasing convergence rates are associated with increasing strength, hence larger differential stresses can be supported as strain rate increases. An increase in temperature with depth favors plastic deformation mechanisms. Ductile strength decreases exponentially with depth and stress relaxes due to aseismic creep [52, 46, 47]. The switching point from brittle slip to creep at depth is defined as the brittle-ductile transition (BDT) [53] and it corresponds with the maximum differential stress supported by rocks in their stability field (Figure .2b).

The 2D numerical model was created using the thermo-mechanical code LAPEX-2D [54, 55]. This software permits modelling of realistic temperature- and stress-dependent viscoelastic rheology combined with Mohr-Coulomb plasticity [56]. At each calculation step (6.12×10^{-4} kyr), the algorithm automatically selects the more appropriate rheology (elasto-plastic or non-linear visco-elastic) at the current conditions of temperature and strain rate (see reference [54] for detailed description of the algorithm and the choice of time step value). The model allows evaluation of rheological profiles through the variation of convergence rates as initial boundary condition. Modelled geometries describe a 2D portion of wet-quartzitic upper crust 250 km wide and 40 km thick, cut by a fault with different dip values in the range of 15-40 degrees (Figure .2a). Grid resolution is 1×1 km. The non-Newtonian power-law viscosity (η) is calculated as

$$\eta = (\frac{1}{2})B^{-1/n}(\varepsilon_{II})^{1/n-1}exp(Q/(nRT)d^{m} \qquad (1)$$

where B, n and Q are parameters, ε_{II} is the second invariant of strain rate, R is the gas constant, d^m (with m=0 [57]) is the grain size and T is the temperature [54]. Implemented rheological parameters are from [58] and listed in Table 2. The initial temperature distribution of the reference model grows from 0 °C at the surface up to 500 °C at the bottom of the domain (40 km depth) following a steady state continental geotherm [59]. To test effects of the local geothermal gradient, the temperature at the bottom was varied between 400 and 600 °C (Figure .2c), i.e. within the typical range at 40 km depth within the continental lithosphere [60].

According to previous studies [61, 62, 63] the fault decoupling is simulated via a 2 km thick weak zone, whose weakness is obtained assuming a lower friction angle and cohesion within the fault domain. Sensitivity of results to fault friction angle (3 to 30 degrees), cohesion (0 to 10 MPa [64]) and grain size of the domain (1 to 3 mm) are shown (Figure .2c). Shortening is simulated via fixed velocities at the left boundary of the model. Hydrostatic pressure is applied at the bottom while other boundaries are left free. A set of models was run for all considered fault dip values (15-40 degrees) and assuming convergence rates varying between 1 and 10 cm/yr. The model evolution time is 100 kyr providing that the steady state of the solution is largely achieved.

3. Results

Figure .3a presents the calculated strain rate after 50 kyr of shortening at 1 cm/yr (upper panel) and 10 cm/yr (lower panel) respectively, for a reference model considering a 20 degrees dipping fault. Both results show that strain focuses along the fault zones with rates of 10^{-13} s^{-1} and 10^{-12} s^{-1} on average. The faster the convergence rate, the deeper the deformation zone propagates (down to 10 km and to 20 km). The point of the model that records the maximum value of differential stress (purple stars in Figure .3a) is assumed as the location of the brittle-ductile transition depth for that solution. Plotting BDT depths vs their location for all the models, it can be recognized a transition band (pink area in Figure .3b) that includes the whole set of BDT points obtained with our calculations for the reference model. The transitional band is laterally delimited by the faults traces with steeper (40°) and shallower (15°) dip angles. Top and bottom limits are isolines, which combine the points of maximum differential stress obtained by models characterized by shortening rates of 1 cm/yr (up) and 10 cm/yr (down) respectively. It is evident that, depending on the shortening rate, BDT depths increase from minimum values of 4-8 km (at 1 cm/yr) to maximum values of 16-18 km (at 10 cm/yr). This range of variation is very sensitive to the fault geometry being larger for shallow dip faults (Figure .3b and S1). In fact, the upper limit occurs at depths of 4 km, 9 km and 13 km in case of fault dipping 15°, 20° or 25° respectively, while the lower limit moves upward from 18 km to 16 km depths increasing the dip angle to 25°. In case of steeper (25°-40°) faults the range of the resulting BDT depths becomes steady (12-17 km). Results show low sensitivity to parameters variation (Figure .3c).

The BDT depths remain comparable to those obtained with the reference model if the grain size for the domain (from 1 to 3 mm) or the fault strength (i.e., cohesion from 0 to 10 MPa) are increased. Results are more sensitive to the initial temperature profile (shallower BDTs are obtained assuming cooler crust) and to the friction angle (narrower and shallower BDT depth for increasing angle) assigned to the fault especially at slow convergence rates (see error bars in figure .3c).

4. Discussion

The results of numerical models dedicated to contractional tectonic settings with variable convergence rates show that the faster the convergence, the deeper the BDT (Figure .3a). A ten times faster shortening (from 1 to 10 cm/yr) generates a doubling of the BDT depth (from 10 to 20 km). This BDT depth variation is mainly controlled by the thermal structure of the crust that results for increasing convergence rates. Faster convergence produces lower temperatures at depth. Lower temperature at depth induces deeper BDT (figure .3c). These values are consistent with observations from fold-and-thrust belts and intraplate contractional areas. As examples, in regions characterized by convergence rates of few mm/yr like Emilia (Italy) (that experienced a seismic sequence in 2012 [65]) or the New Madrid seismic zone [66], brittle deformation is confined at depths of 10-15 km. This value fits the depth of the decollement constrained by geological data for both the N-Apennines [67] and the New Madrid area [68], although they belong to different tectonic systems (fold-and thrust belt and intraplate region respectively). The BDT depth decreases up to few kilometers for even smaller shortening rates (Figure S2). Where the India plate converges with Eurasia at rates of 4-6 cm/yr, the BDT is well defined at depth of 15-16 km [69, 70]. Intraplate earthquakes around the descending oceanic plate at the Japan plate boundary (converging at 10 cm/yr) illuminate a seismogenic volume down to 25 km [71], comparable with the $\simeq$ 20 km obtained from our models.

Unlike earthquakes due to extensional tectonics operating in favor of gravity (graviquakes [5]), the physics behind earthquakes in thrust settings (elastoquakes) requires much more energy to activate the process. In fact, thrust earthquakes not only need to overcome the static friction over the fault but enough energy to lift up the involved seismic volume is also required. Moreover, the fault length/depth ratio (hence the volume) increases moving from normal ($\simeq$ 3) to strike-slip ($\simeq$ 10) and thrust faults ($\simeq$ 25) [5]). This explains why the largest magnitudes worldwide are recorded at convergent plate boundaries (Figure .1a).

Deeper BDT depths imply larger brittle volumes that have to be mobilized by tectonic processes (Table 3), and thus necessitate greater energy storage; the deeper the BDT, the larger the magnitude of the expected earthquake. The seismogenic depth-convergence rate relationship highlighted in this work allows calculation of the volumes potentially involved during the coseismic slip (grey prism in Fig. .4). The distance from the frontal thrust to the internal conjugate margin ((i.e., the width W in Figure .4) is derived assuming that the frontal thrust and the conjugate fault are perpendicular. The volume length (L_f in figure .4) is assumed to be 25 times the BDT depth. Following the approach in [6] the brittle volume (V_b) is defined from

BDT depth (z_{bdt}), fault dip (α) and rupture length (L_f) as:

$$V_b = L_f \ (\frac{3}{2} \ z_{bdt}^3 \ [cot(\alpha) + cot(90 - \alpha)] \tag{2}$$

BDT depth and fault dips are those from calculations. Considering low angle faults dipping at 15°- 20°, involved volumes grow very fast from $\simeq$ 3-4 $\times$ 10^4 km^3 at 1 cm/yr to $\simeq$ 15-19 $\times$ 10^4 km^3 at 10 cm/yr (see table 3). In case of faults dipping in the range of 25°- 40°, calculated volumes increase slowly but considerably by 2 $\times$ 10^4 km^3 with convergence rate. Overall, depending on the convergence rate, an increase of the volume involved during a seismic event between 2 $\times$ 10^4 km^3 and 10 $\times$ 10^4 km^3 can be predicted for thrust faults. This volume increase is remarkable if we consider that the slip of $10^5 km^3$ of rocks could potential produce a Mw>8.0 earthquake [5, 6]. Available empirical relationships correlating seismic volumes and earthquakes magnitude [7, 8] allow to derive a magnitude increase of between 1 and 2 times with BDT deepening 5-15 km (Figure .5).

Using relationship (1) and assuming a steep thrust (with a dip of 40°), a doubling of the BDT depth, obtained increasing convergence rate from 1 to 10 cm/yr, is associated with an eightfold increase of the volume (BDT 10 km = mobilized volume 25.000 km^3; BDT 20 km = mobilized volume 200.000 km^3). Shallow dip (dip of 15°) thrusts are characterized by larger distance between the hypocenter and the conjugate backstop, with a significant increment of the volume (e.g., BDT at 10 km = mobilized volume of 50.000 km^3; BDT at 20 km = mobilized volume of 400.000 km^3; Figure .5 and table 3).

This value may diminish considering that the transition between creeping and locked portions of thrusts does not necessarily coincide with the BDT.

Also local variations in the fault parameters could affect this value (Figure .3c). In particular, it could be shallower when evaporitic layers behave as decollement or when shaly layers have mineralogy that may control the differential frictional behavior, e.g. the Ca-smectite transformation in illite, or other lithological variations that may further control the behavior of regional thrust planes [72].

It is worth mentioning that the geometries resulting from thrust propagation are generally considered to be controlled by mechanical properties of rocks or to fault geometry [73, and references therein]. Shortening rate here analyzed could also be a primary factor. For slow convergence, blind thrusts and small co-seismic slips are expected to occur. In this case, fault propagation at depth is possibly associated with a fault propagation fold [74] at the surface (Figure .6a). Blind faults are typical in regions characterized by convergence rates of few mm/yr, like Italy [75, 76]. At fast convergence rates (i.e., 10 cm/yr like Japan [39, 43]) thrust faults propagate to the surface involving larger portion of the fault [77]. In this case, fault bend faults [78] are passively generated due to undulations in the fault plane (Figure .6b).

5. Conclusions

Comparing GPS data and available regional studies it is observed that the seismogenic layer (delimited at depth by the BDT) thickens with increasing convergence rates. This trend is confirmed by 2D thermo-mechanical models of thrust faults, showing that BDT depths double (from 7-8 km up to 15 km) when increasing convergence rate from 1 to 10 cm/yr. In addition to convergence rate, the BDT depth depends on the initial temperature profile and on rheological assumptions (e.g., the fault friction angle).

BDT depths obtained from our calculations were used to derive the maximum brittle volume that may be mobilized during seismic events. This also depends upon convergence rate. A doubling of the BDT depth is associated with a four- to eight-fold increase of the seismogenic volume depending on the fault dip, i.e., an increase of 1-2 in magnitude of the associated earthquake. These results are consistent with global seismic data that show a linear increase between convergence rates and earthquake magnitude for earthquakes nucleated along plate-boundary thrust faults.

Acknowledgements

P.P. thanks Andrey Babeyko for fruitful discussions and for providing the numerical code. Marco Cuffaro is thanked for discussion during early stages of the work. Financial support from PRIN2015-Project 2015EC9PJ5-001 and Progetti di Ateneo Sapienza 2016 (Carlo Doglioni, Cristiano Collettini and Luca Aldega) and 2017 (Eugenio Carminati) is acknowledged. Most figures were created using GMT 5 [79] (http://gmt.soest.hawaii.edu/). All numerical results are available in the journal data repository and upon request from the corresponding author.

Appendix A - Method for GPS velocities

Concerning figure .1, the convergence rates between plate pairs along transects (black lines) were obtained from the most recent kinematic models and velocity solutions. Those involving the Pacific plate are obtained from the Euler poles and rotation rates provided by [80], Table 2, which contains the angular velocities for all the assumed rigid plates included in the Global Strain Rate Model (v.2.1). They are listed relative to the Pacific plate, which is the models reference plate. From this model we have computed the corresponding convergence rates between the following plate pairs: Pacific- North America (Alaska), Pacific-Eurasia (Japan), Pacific-Australia (north and south Tonga). The convergence rate between Juan de Fuca and North America plates (Cascadia) was computed using the additive property of the Euler vectors, each one known with respect to the Pacific plate. A second set of convergence rates was computed from the GPS velocity solutions provided by [81, 82, 83] by removing the Euler rigid rotation of one plate with respect to the other for the following plate pairs; Adria-Eurasia (Alps, north Apennines), Africa-Eurasia (Calabrian Arc), Nazca-South America (Chile), Anatolia-Africa (Hellenic Arc), India-Eurasia, Australia-Eurasia (Java-Sumatra) and Arabia-Eurasia (Zagros). All the rates best represent the inter-seismic relative plate velocity around the area of transects, since they are free from seismic and post-seismic non-linear behaviors; they have only a local validity since they are obtained as projection of spherical motion on the tangent plane. The rates are reported without uncertainties as they are not directly derived from measurements (Table 1).

References

[1] D. L. Wells, K. J. Coppersmith, New empirical relationships among magnitude, rupture length, rupture width, rupture area, and surface displacement, Bulletin of the seismological Society of America 84 (4) (1994) 974–1002.

[2] P. M. Mai, G. C. Beroza, Source scaling properties from finite-fault-rupture models, Bulletin of the Seismological Society of America 90 (3) (2000) 604–615. doi:10.1785/0119990126.

[3] T. C. Hanks, W. H. Bakun, A bilinear source-scaling model for m-log a observations of continental earthquakes, Bulletin of the Seismological Society of America 92 (5) (2002) 1841–1846. doi:10.1785/0120010148.

[4] M. Leonard, Earthquake fault scaling: Self-consistent relating of rupture length, width, average displacement, and moment release, Bulletin of the Seismological Society of America 100 (5A) (2010) 1971–1988. doi:10.1785/0120090189.

[5] C. Doglioni, E. Carminati, P. Petricca, F. Riguzzi, Normal fault earthquakes or graviquakes, Scientific Reports 5 (12110) (2015) 1–12. doi:10.1038/srep12110, (2015a).

[6] P. Petricca, S. Barba, E. Carminati, C. Doglioni, F. Riguzzi, Graviquakes in italy, Tectonophysics 656 (2015) 202–214. doi:10.1016/j.tecto.2015.07.001.

[7] M. Bath, S. Duda, Earthquake volume, fault plane area, seismic energy,

strain, deformation and related quantities, Annals of Geophysics 17 (3) (1964) 353–368.

[8] C. Doglioni, S. Barba, E. Carminati, F. Riguzzi, Fault on-off versus strain rate and earthquakes energy, Geoscience Frontiers 6 (2) (2015) 265–276. doi:10.1016/j.gsf.2013.12.007.

[9] P. Bird, Y. Kagan, D. Jackson, F. Schoenberg, M. Werner, Linear and nonlinear relations between relative plate velocity and seismicity, Bulletin of the Seismological Society of America 99 (6) (2009) 3097–3113. doi:10.1785/0120090082.

[10] S. Ide, The proportionality between relative plate velocity and seismicity in subduction zones, Nature Geoscience 6 (9) (2013) 780. doi:10.1038/NGEO1901.

[11] L. Ruff, H. Kanamori, Seismicity and the subduction process, Physics of the Earth and Planetary interiors 23 (3) (1980) 240–252.

[12] C. Doglioni, S. Barba, E. Carminati, F. Riguzzi, Role of the brittle–ductile transition on fault activation, Physics of the Earth and Planetary Interiors 184 (3-4) (2011) 160–171. doi:10.1016/j.pepi.2010.11.005.

[13] P. Bird, Y. Y. Kagan, Plate-tectonic analysis of shallow seismicity: Apparent boundary width, beta, corner magnitude, coupled lithosphere thickness, and coupling in seven tectonic settings, Bulletin of the Seismological Society of America 94 (6) (2004) 2380–2399. doi:10.1785/0120030107.

[14] C. Chiarabba, P. De Gori, The seismogenic thickness in italy: constraints on potential magnitude and seismic hazard, Terra Nova 28 (6) (2016) 402–408. doi:10.1111/ter.12233.

[15] D. A. Storchak, D. Di Giacomo, I. Bondr, E. R. Engdahl, J. Harris, W. H. K. Lee, A. Villaseor, P. Bormann, Public release of the iscgem global instrumental earthquake catalogue (19002009), Seismological Research Letters 84 (5) (2013) 810. doi:10.1785/0220130034.

[16] K. K. S. Thingbaijam, P. Martin Mai, K. Goda, New empirical earthquake source-scaling laws, Bulletin of the Seismological Society of America 107 (5) (2017) 2225–2246. doi:10.1785/0120170017.

[17] C. H. Scholz, C. Aviles, S. G. Wesnousky, Scaling differences between large interplate and intraplate earthquakes, Bulletin of the Seismological Society of America 76 (1) (1986) 65–70.

[18] K. Wang, Y. Hu, J. He, Deformation cycles of subduction earthquakes in a viscoelastic earth, Nature 484 (7394) (2012) 327. doi:10.1038/nature11032.

[19] X. Gao, K. Wang, Rheological separation of the megathrust seismogenic zone and episodic tremor and slip, Nature 543 (7645) (2017) 416. doi:10.1038/nature21389.

[20] T. I. Allen, G. P. Hayes, Alternative rupture-scaling relationships for subduction interface and other offshore environments, Bulletin of the Seismological Society of America 107 (3) (2017) 1240–1253. doi:10.1785/0120160255.

[21] F. O. Strasser, M. Arango, J. J. Bommer, Scaling of the source dimensions of interface and intraslab subduction-zone earthquakes with moment magnitude, Seismological Research Letters 81 (6) (2010) 941–950. doi:10.1785/gssrl.81.6.941.

[22] L. Dal Zilio, Y. van Dinther, T. V. Gerya, C. C. Pranger, Seismic behaviour of mountain belts controlled by plate convergence rate, Earth and Planetary Science Letters 482 (2018) 81–92. doi:10.1016/j.epsl.2017.10.053.

[23] L. Ruff, H. Kanamori, Seismic coupling and uncoupling at subduction zones, Tectonophysics 99 (2-4) (1983) 99–117. doi:10.1016/0040-1951(83)90097-5.

[24] C. Kreemer, W. E. Holt, A. J. Haines, An integrated global model of present-day plate motions and plate boundary deformation, Geophysical Journal International 154 (1) (2003) 8–34. doi:10.1046/j.1365-246X.2003.01917.x.

[25] J. F. Pacheco, L. R. Sykes, C. H. Scholz, Nature of seismic coupling along simple plate boundaries of the subduction type, Journal of Geophysical Research: Solid Earth 98 (B8) (1993) 14133–14159. doi:10.1029/93JB00349.

[26] W. Schellart, N. Rawlinson, Global correlations between maximum magnitudes of subduction zone interface thrust earthquakes and physical parameters of subduction zones, Physics of the Earth and Planetary Interiors 225 (2013) 41–67. doi:10.1016/j.pepi.2013.10.001.

[27] F. Corbi, R. Herrendoerfer, F. Funiciello, Y. Van Dinther, Controls of seismogenic zone width and subduction velocity on interplate seismicity: insights from analog and numerical models, Geophysical Research Lettersdoi:10.1002/2016GL072415.

[28] R. McCaffrey, Influences of recurrence times and fault zone temperatures on the age-rate dependence of subduction zone seismicity, Journal of Geophysical Research: Solid Earth 102 (B10) (1997) 22839–22854. doi:10.1029/97JB01827.

[29] R. McCaffrey, Statistical significance of the seismic coupling coefficient, Bulletin of the Seismological Society of America 87 (4) (1997) 1069.

[30] A. Heuret, S. Lallemand, F. Funiciello, C. Piromallo, C. Faccenna, Physical characteristics of subduction interface type seismogenic zones revisited, Geochemistry, Geophysics, Geosystems 12 (1). doi:10.1029/2010GC003230.

[31] B. W. Tichelaar, L. J. Ruff, Depth of seismic coupling along subduction zones, Journal of Geophysical Research: Solid Earth 98 (B2) (1993) 2017–2037. doi:10.1029/92JB02045.

[32] D. Oleskevich, R. Hyndman, K. Wang, The updip and downdip limits to great subduction earthquakes: Thermal and structural models of cascadia, south alaska, sw japan, and chile, Journal of Geophysical Research: Solid Earth 104 (B7) (1999) 14965–14991. doi:10.1029/1999JB900060.

[33] R. Devoti, F. Riguzzi, M. Cuffaro, C. Doglioni, New gps constraints

on the kinematics of the apennines subduction, Earth and Planetary Science Letters 273 (1-2) (2008) 163–174. doi:10.1016/j.epsl.2008.06.031.

[34] L. Minelli, C. Faccenna, Evolution of the calabrian accretionary wedge (central mediterranean), Tectonics 29 (4). doi:10.1029/2009TC002562.

[35] A. Polonia, L. Torelli, P. Mussoni, L. Gasperini, A. Artoni, D. Klaeschen, The calabrian arc subduction complex in the ionian sea: Regional architecture, active deformation, and seismic hazard, Tectonics 30 (5). doi:10.1029/2010TC002821.

[36] A. Maggi, J. Jackson, K. Priestley, C. Baker, A re-assessment of focal depth distributions in southern iran, the tien shan and northern india: Do earthquakes really occur in the continental mantle?, Geophysical Journal International 143 (3) (2000) 629–661. doi:10.1046/j.1365246X.2000.00254.x.

[37] A. Maggi, J. Jackson, D. Mckenzie, K. Priestley, Earthquake focal depths, effective elastic thickness, and the strength of the continental lithosphere, Geology 28 (6) (2000) 495–498. doi:10.1130/0091-7613(2000)28¡495:EFDEET¿2.0.CO;2.

[38] C. Chen, D. Zhao, S. Wu, Tomographic imaging of the cascadia subduction zone: constraints on the juan de fuca slab, Tectonophysics 647 (2015) 73–88. doi:10.1016/j.tecto.2015.02.012.

[39] P. A. McCrory, R. D. Hyndman, J. L. Blair, Relationship between the cascadia fore-arc mantle wedge, nonvolcanic tremor, and the downdip

limit of seismogenic rupture, Geochemistry, Geophysics, Geosystems 15 (4) (2014) 1071–1095. doi:10.1002/2013GC005144.

[40] S. Hippchen, R. Hyndman, Thermal and structural models of the sumatra subduction zone: Implications for the megathrust seismogenic zone, Journal of Geophysical Research: Solid Earth 113 (B12). doi:10.1029/2008JB005698.

[41] R. Collings, D. Lange, A. Rietbrock, F. Tilmann, D. Natawidjaja, B. Suwargadi, M. Miller, J. Saul, Structure and seismogenic properties of the mentawai segment of the sumatra subduction zone revealed by local earthquake traveltime tomography, Journal of Geophysical Research: Solid Earth 117 (B1). doi:10.1029/2011JB008469.

[42] M. Pérez-Gussinyé, A. Lowry, J. Phipps Morgan, A. Tassara, Effective elastic thickness variations along the andean margin and their relationship to subduction geometry, Geochemistry, Geophysics, Geosystems 9 (2). doi:10.1029/2007GC001786.

[43] A. Tanaka, Y. Ishikawa, Crustal thermal regime inferred from magnetic anomaly data and its relationship to seismogenic layer thickness: The japanese islands case study, Physics of the Earth and Planetary Interiors 152 (4) (2005) 257–266. doi:10.1016/j.pepi.2005.04.011.

[44] S. M. Peacock, Blueschist-facies metamorphism, shear heating, and p-t-t paths in subduction shear zones, Journal of Geophysical Research: Solid Earth 97 (B12) (1992) 17693–17707. doi:10.1029/92JB01768.

[45] X. Deng, M. B. Underwood, Abundance of smectite and the location of a plate-boundary fault, barbados accretionary prism, Geological Society of America Bulletin 113 (4) (2001) 495–507. doi:10.1130/0016-7606(2001)113¡0495:AOSATL¿2.0.CO;2.

[46] R. H. Sibson, Continental fault structure and the shallow earthquake source, Journal of the Geological Society 140 (5) (1983) 741–767. doi:10.1144/gsjgs.140.5.0741.

[47] C. Scholz, The brittle-plastic transition and the depth of seismic faulting, Geologische Rundschau 77 (1) (1988) 319–328.

[48] T. J. Ahrens, Rock physics & phase relations: A handbook of physical constants, American Geophysical Union, 1995.

[49] J. Keefner, S. Mackwell, D. Kohlstedt, F. Heidelbach, Dependence of dislocation creep of dunite on oxygen fugacity: implications for viscosity variations in earth's mantle, Journal of Geophysical Research: Solid Earth 116 (B5). doi:10.1029/2010JB007748.

[50] R. H. Sibson, Frictional constraints on thrust, wrench and normal faults, Nature 249 (5457) (1974) 542.

[51] G. Hirth, N. M. Beeler, The role of fluid pressure on frictional behavior at the base of the seismogenic zone, Geology 43 (3) (2015) 223–226. doi:10.1130/G36361.1.

[52] R. Sibson, Fault rocks and fault mechanisms, Journal of the Geological Society 133 (3) (1977) 191–213. doi:10.1144/gsjgs.133.3.0191.

[53] S. Schmid, Towards a genetic classification of fault rocks: geological usage and tectonophysical implications, Controversies in modern geology.

[54] A. Y. Babeyko, S. V. Sobolev, R. Trumbull, O. Oncken, L. Lavier, Numerical models of crustal scale convection and partial melting beneath the altiplano–puna plateau, Earth and Planetary Science Letters 199 (3-4) (2002) 373–388. doi:10.1016/S0012-821X(02)00597-6.

[55] S. V. Sobolev, A. Y. Babeyko, What drives orogeny in the andes?, Geology 33 (8) (2005) 617–620. doi:10.1130/G21557AR.1.

[56] O. Zienkiewicz, I. Cormeau, Visco-plasticityplasticity and creep in elastic solidsa unified numerical solution approach, International Journal for Numerical Methods in Engineering 8 (4) (1974) 821–845. doi:10.1002/nme.1620080411.

[57] A. Walker, E. Rutter, K. Brodie, Experimental study of grain-size sensitive flow of synthetic, hot-pressed calcite rocks, Geological Society, London, Special Publications 54 (1) (1990) 259–284. doi:10.1144/GSL.SP.1990.054.01.24.

[58] G. C. Gleason, J. Tullis, A flow law for dislocation creep of quartz aggregates determined with the molten salt cell, Tectonophysics 247 (1-4) (1995) 1–23. doi:10.1016/00401951(95)00011-B.

[59] D. McKenzie, J. Jackson, K. Priestley, Thermal structure of oceanic and continental lithosphere, Earth and Planetary Science Letters 233 (3-4) (2005) 337–349. doi:10.1016/j.epsl.2005.02.005.

[60] N. Kusznir, R. Park, Continental lithosphere strength: the critical role of lower crustal deformation, Geological Society, London, Special Publications 24 (1) (1986) 79–93. doi:10.1144/GSL.SP.1986.024.01.09.

[61] C. Giunchi, R. Sabadini, E. Boschi, P. Gasperini, Dynamic models of subduction: geophysical and geological evidence in the tyrrhenian sea, Geophysical Journal International 126 (2) (1996) 555–578. doi:10.1111/j.1365-246X.1996.tb05310.x.

[62] S. Zhong, M. Gurnis, L. Moresi, Role of faults, nonlinear rheology, and viscosity structure in generating plates from instantaneous mantle flow models, Journal of Geophysical Research: Solid Earth 103 (B7) (1998) 15255–15268. doi:10.1029/98JB00605.

[63] E. Carminati, P. Petricca, State of stress in slabs as a function of large-scale plate kinematics, Geochemistry, Geophysics, Geosystems 11 (4). doi:10.1029/2009GC003003.

[64] P. Jeanne, Y. Guglielmi, F. Cappa, Multiscale seismic signature of a small fault zone in a carbonate reservoir: Relationships between vp imaging, fault zone architecture and cohesion, Tectonophysics 554 (2012) 185–201. doi:10.1016/j.tecto.2012.05.012.

[65] S. Pondrelli, S. Salimbeni, P. Perfetti, P. Danecek, Quick regional centroid moment tensor solutions for the emilia 2012 (northern italy) seismic sequence, Annals of Geophysics 55 (4).

[66] M. Zoback, R. Hamilton, A. Crone, D. Russ, F. McKeown, S. Brockman,

Recurrent intraplate tectonism in the new madrid seismic zone, Science 209 (4460) (1980) 971–976. doi:10.1126/science.209.4460.971.

[67] E. Carminati, D. Scrocca, C. Doglioni, Compaction-induced stress variations with depth in an active anticline: Northern apennines, italy, Journal of Geophysical Research: Solid Earth 115 (B2). doi:10.1029/2009JB006395.

[68] L. Liu, M. D. Zoback, Lithospheric strength and intraplate seismicity in the new madrid seismic zone, Tectonics 16 (4) (1997) 585–595. doi:10.1029/97TC01467.

[69] H. Bungum, C. D. Lindholm, A. K. Mahajan, Earthquake recurrence in nw and central himalaya, Journal of Asian Earth Sciences 138 (2017) 25–37. doi:10.1016/j.jseaes.2017.01.034.

[70] P. K. Gautam, V. Gahalaut, S. K. Prajapati, N. Kumar, R. K. Yadav, N. Rana, C. P. Dabral, Continuous gps measurements of crustal deformation in garhwal-kumaun himalaya, Quaternary International 462 (2017) 124–129. doi:10.1016/j.quaint.2017.05.043.

[71] T. Igarashi, T. Matsuzawa, N. Umino, A. Hasegawa, Spatial distribution of focal mechanisms for interplate and intraplate earthquakes associated with the subducting pacific plate beneath the northeastern japan arc: A triple-planed deep seismic zone, Journal of Geophysical Research: Solid Earth 106 (B2) (2001) 2177–2191. doi:10.1029/2000JB900386.

[72] T. Hirono, K. Tsuda, W. Tanikawa, J.-P. Ampuero, B. Shibazaki, M. Kinoshita, J. J. Mori, Near-trench slip potential of megaquakes evaluated

from fault properties and conditions, Scientific reports 6 (2016) 28184. doi:10.1038/srep28184.

[73] A. N. Hughes, N. P. Benesh, J. H. Shaw, Factors that control the development of fault-bend versus fault-propagation folds: Insights from mechanical models based on the discrete element method (dem), Journal of Structural Geology 68 (2014) 121–141. doi:10.1016/j.jsg.2014.09.009.

[74] J. Suppe, D. A. Medwedeff, Geometry and kinematics of fault-propagation folding, Eclogae Geologicae Helvetiae 83 (3) (1990) 409–454.

[75] P. Burrato, F. Ciucci, G. Valensise, An inventory of river anomalies in the po plain, northern italy: evidence for active blind thrust faulting, Annals of Geophysics.

[76] P. Vannoli, R. Basili, G. Valensise, New geomorphic evidence for anticlinal growth driven by blind-thrust faulting along the northern marche coastal belt (central italy), Journal of Seismology 8 (3) (2004) 297–312. doi:10.1023/B:JOSE.0000038456.00574.e3.

[77] S. Kodaira, Y. Nakamura, Y. Yamamoto, K. Obana, G. Fujie, T. No, Y. Kaiho, T. Sato, S. Miura, Depth-varying structural characters in the rupture zone of the 2011 tohoku-oki earthquake, Geosphere 13 (5) (2017) 1408–1424. doi:10.1130/GES01489.1.

[78] J. Suppe, Geometry and kinematics of fault-bend folding, American Journal of science 283 (7) (1983) 684–721.

[79] P. Wessel, W. H. Smith, R. Scharroo, J. Luis, F. Wobbe, Generic mapping tools: improved version released, Eos, Transactions American Geophysical Union 94 (45) (2013) 409–410.

[80] C. Kreemer, G. Blewitt, E. C. Klein, A geodetic plate motion and global strain rate model, Geochemistry, Geophysics, Geosystems 15 (10) (2014) 3849–3889. doi:10.1002/2014GC005407.

[81] R. Devoti, N. D´ Agostino, E. Serpelloni, G. Pietrantonio, F. Riguzzi, A. Avallone, A. Cavaliere, D. Cheloni, G. Cecere, C. D´ Ambrosio, L. Falco, G. Selvaggi, M. Métois, A. Esposito, V. Sepe, A. Galvani, M. Anzidei, The mediterranean crustal motion map compiled at ingv, Annals of Geophysics 60 (2) (2017) 163–174. doi:DOI:10.4401/ag-7059.

[82] X. Le Pichon, C. Kreemer, The miocene-to-present kinematic evolution of the eastern mediterranean and middle east and its implications for dynamics, Annual Review of Earth and Planetary Sciences 38 (2010) 323–351.

[83] Z. Altamimi, L. Métivier, X. Collilieux, ITRF2008 plate motion model, Journal of Geophysical Research: Solid Earth 117 (B7). doi:10.1029/2011JB008930.

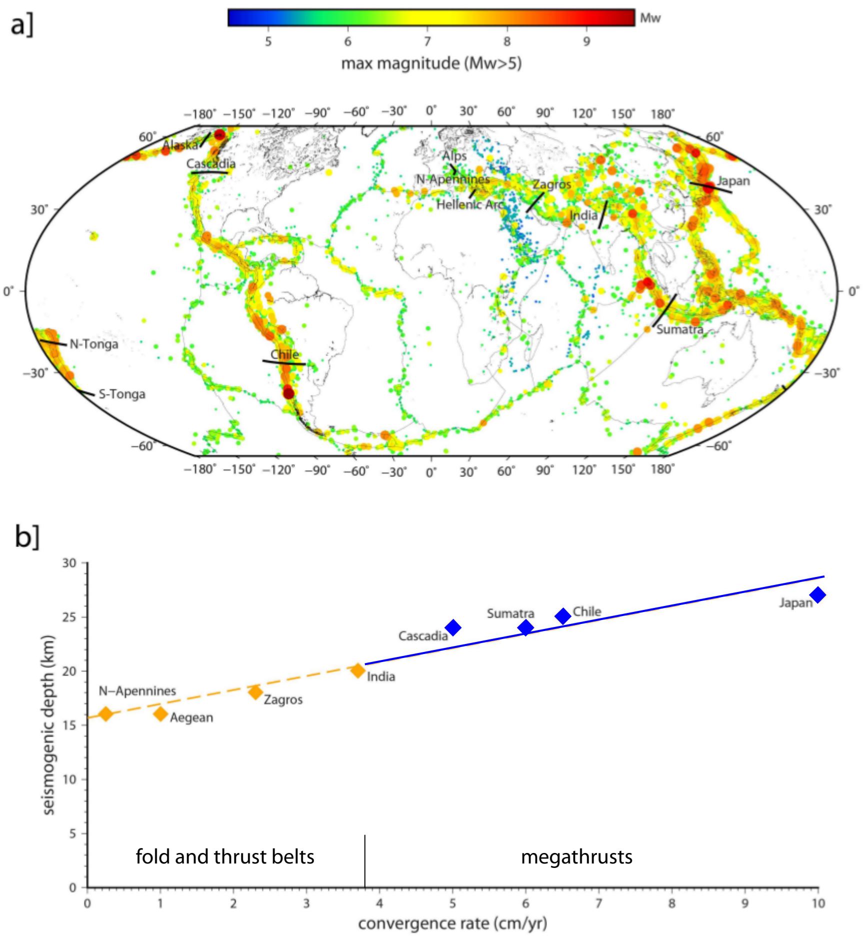

Figure .1: **a**] Map showing geographical distribution and magnitude of the global earthquakes (M> 5) for the period 1900-2013 from the ISC-GEM catalog update of January 2017 (version 4.0) [15]. Black lines represent transects where convergence rates across selected plate boundaries were calculated (appendix A) and plotted versus maximum seismogenic depths in panel **b**]. Note that the locations of the largest earthquakes (orange-red dots in panel **a**]) correspond to realms characterized by higher rates of convergence. Panel **b**]: the maximum seismogenic depth increases from 15 km at slowly converging regions (1-4 cm/yr) in fold and thrust belts (yellow diamonds) down to 25 km along faster converging boundaries (5-10 cm/yr) at subduction boundaries (blue diamonds).

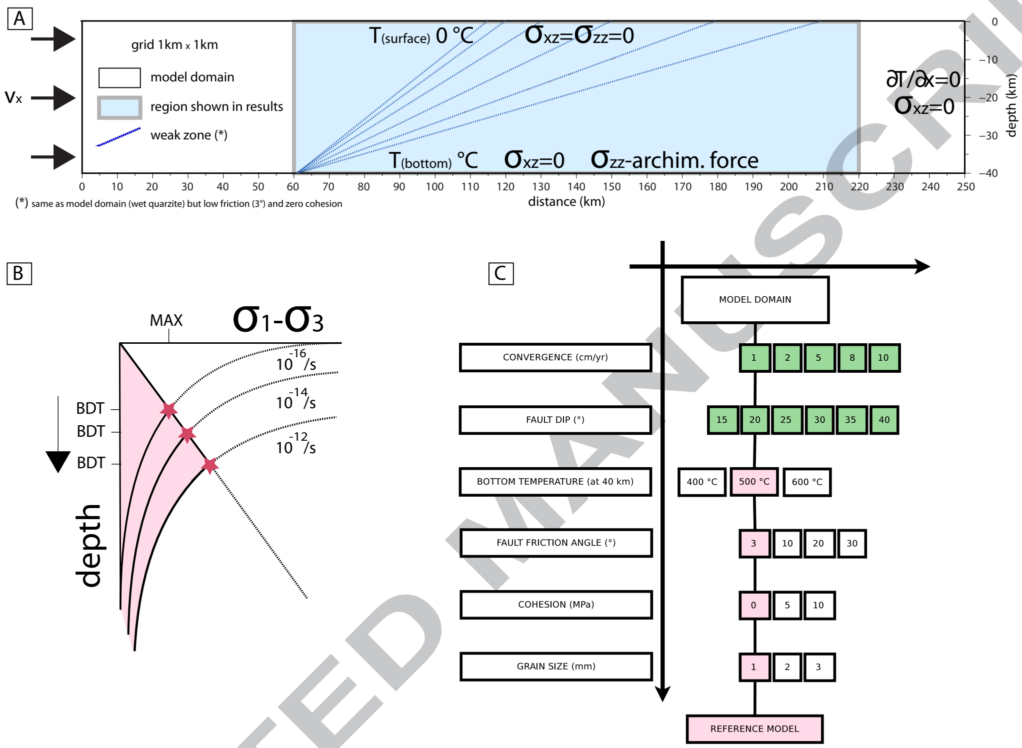

Figure .2: **Setup of numerical models.** **A**] Geometry and boundary conditions (see the main text for description). **B**] Panel showing the brittle-ductile transition (BDT) depth (purple star) defined by the point of maximum differential stress and depending on the applied strain rate. **C**] Diagram showing the range of variation for different parameters utilized in the model. Pink and green boxes highlight parameters utilized in the reference model (see table 2). Our modelling strategy requires that only one sensitivity parameter (white boxes) per run was changed with respect to reference parameters (pink boxes). All simulations provide results for each test parameter (green boxes).

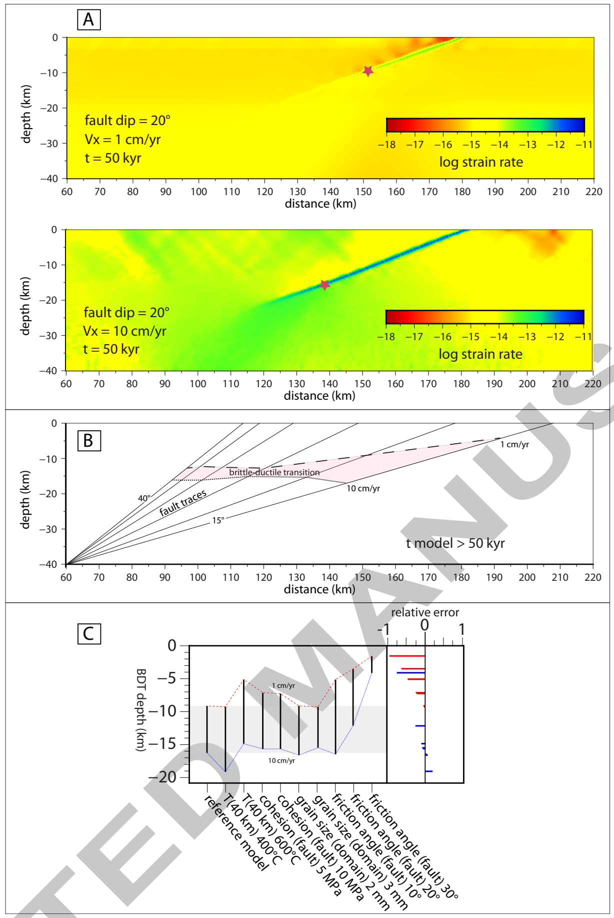

Figure .3: **Main results of numerical models. A**] Results of reference model showing the strain rate after 50 kyr considering a 20° dipping fault and forcing a convergence rate of 1 cm/yr (upper panel) and 10 cm/yr (lower panel). The brittle-ductile transition (BDT) depth (purple star) corresponds to the point of maximum differential stress of the model (Figure .2b) and deepens along the fault (area of maximum strain rate) by increasing the convergence rate (BDT at 10 km and at 20 km for rates of 1 cm/yr and 10 cm/yr respectively). **B**] Distribution of BDT depths (pink area) from results of the whole set of models with reference parameters values (pink boxes in figure .2c)). Notice that beside convergence rate, fault dip controls the range of variation of the BDT depth values being greater for shallow dipping faults (depth varies until $\simeq$ 12 km if the fault dips 15° and $\simeq$ 5 km if the fault dips 40° depending on forced convergence rate). **C**] Results obtained varying the sensitivity parameters and comparison with BDT depths calculated at different convergence rates for the reference model (gray area). Corresponding relative errors are also shown in red and blue for results obtained assuming 1 and 10 cm/yr of convergence respectively.

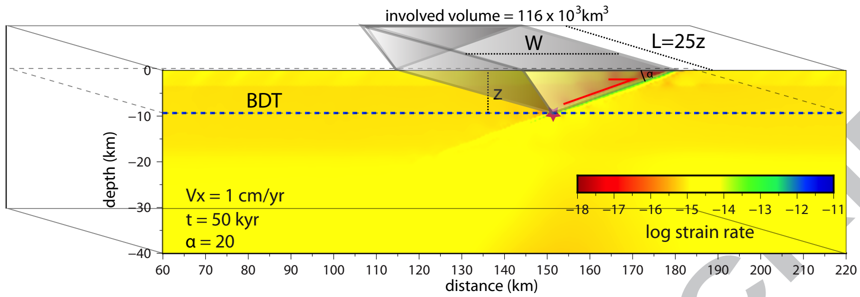

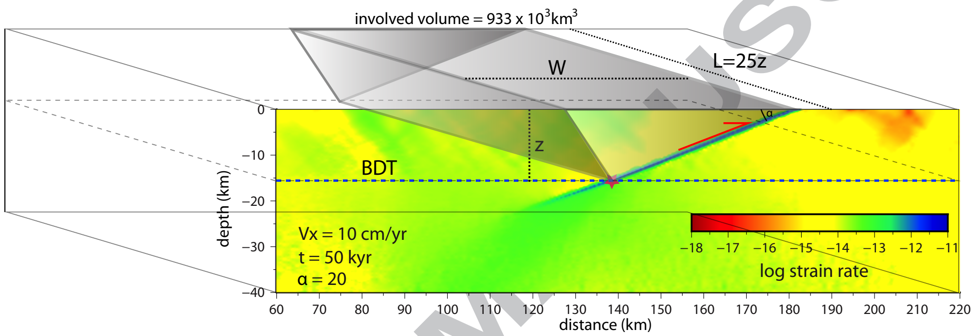

Figure .4: **Sketch showing the volume involved in thrust faults earthquakes depending on BDT depth, hence on convergence rate.** The doubling of the BDT depth determines an increase of the volume of at least four times, corresponding to an increase of 2 orders of magnitude of the released energy.

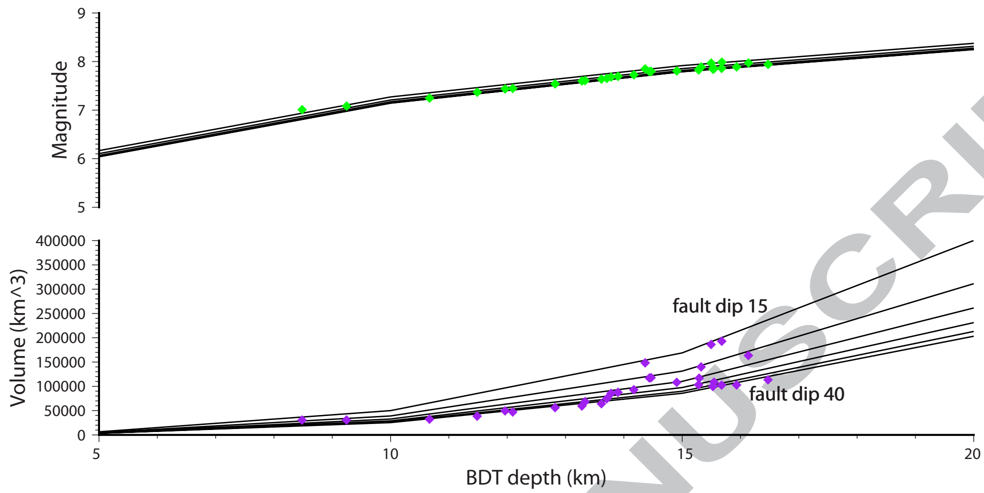

Figure .5: **BDT depth vs seismic volume and magnitude.** The volume theoretically mobilized during thrust earthquakes (lower panel) is calculated from the BDT depth using the equation in [6] for different fault dips. The related magnitudes (upper panel) are calculated with the equation proposed in [8] and show an increase of 2 when the BDT depth deepens from 5 km to 20 km. Purple and green diamonds refer to BDT depths obtained with our models. Notice that magnitude is more sensitive to BDT rather than to fault dip changes.

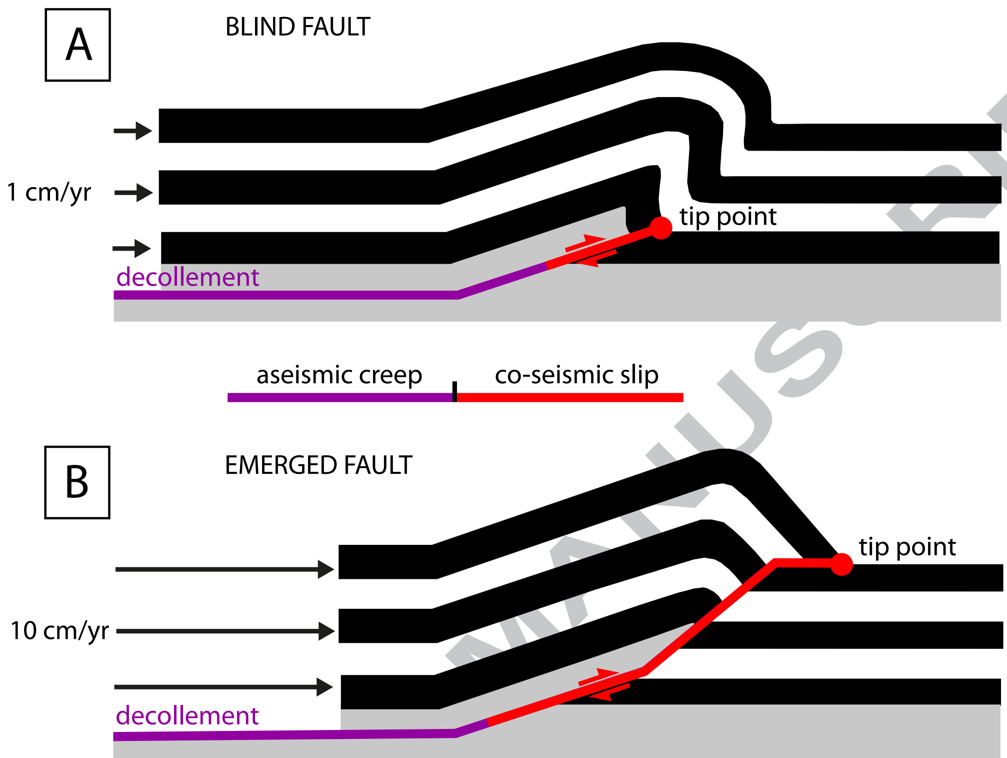

Figure .6: **Thrust-related geometries in slow and fast convergence realms. A]** At slow convergence rates, the small amount of co-seismic slip generates a blind thrust whereas deformation is accommodated at shallower depths by the development of a fault propagation fold. **B]** At fast convergence rates, the thrust failure propagates to the surface and a fault-bend-fold is passively generated.

subduction	rate (mm/yr)	plate pairs	source ref.
Alps	2.0	AD-EU	51
N-Apennines	2.5	EU-AD	51
Calabrian Arc	5.0	AF-EU	51
Hellenic Arc	34.0	AN-AF	52
Zagros	23.0	AR-EU	52
India	37.0	IN-EU	52
Java-Sumatra	60.0	AU-EU	53
Tonga S	49.0	AU-PA	54
Tonga N	76.0	AU-PA	54
Japan	100.0	EU-PA	54
Alaska	58.0	NA-PA	54
Cascadia	50.0	JF-NA	54
Chile	65.0	NZ-SA	53

Table 1. Convergence rates calculated along transects shown in Figure 1.

parameter		**unit**	**value**
density (at 20°C and 1 bar)	ρ	kg/m^3	2800
thermal expansion	α	K^{-1}	3.7×10^{-5}
bulk modulus	K	GPa	55
shear modulus	G	GPa	36
heat capacity	C_p	$J/kg/K$	1200
heat conductivity	λ	$W/K/m$	2.5
heat productivity	A	$\mu W/m^3$	1.5
creep activation energy	Q	kJ/mol	223
pre-exponential multiplier	$log(B)$	$Pa^{-n}s^{-1}$	-28
power-law exponent	n		4
Mohr-Coulomb elasto-plasticity			
domain: friction angle		$^\circ$	30
cohesion		MPa	10
weak zone: friction angle		$^\circ$	3
cohesion		MPa	0

Table 2. Values and parameters used in the reference model.

dip	vel. (mm/yr)	$\sigma 1 - \sigma 3_{max}$ (MPa)	BDTz (km)	V (km^3)	M
15	1	91.9	4.4	4361	6.0
20	1	126.2	9.2	30750	7.1
25	1	239.2	15.3	116777	7.9
30	1	259.5	15.3	103098	7.8
35	1	277.4	15.7	102567	7.9
40	1	295.3	16.5	113546	7.9
15	2	199.3	8.5	30536	7.0
20	2	262.9	15.3	140074	7.9
25	2	428.6	13.8	85462	7.7
30	2	335.0	13.3	68497	7.6
35	2	312.0	12.1	47103	7.4
40	2	345.7	13.3	59516	7.6
15	5	437.1	14.4	148301	7.8
20	5	432.0	16.1	163516	8.0
25	5	394.5	14.2	92944	7.7
30	5	348.5	12.0	49472	7.4
35	5	359.7	10.7	32307	7.2
40	5	356.6	11.5	38484	7.4
15	8	466.8	15.5	186182	8.0
20	8	392.6	14.4	117149	7.8
25	8	392.1	13.9	87698	7.7
30	8	415.4	13.7	74417	7.7
35	8	396.6	12.8	56107	7.5
40	8	417.1	13.6	64116	7.6
15	10	502.1	15.7	192864	8.0
20	10	428.1	14.5	117844	7.8
25	10	397.1	14.9	108192	7.8
30	10	437.1	15.5	108550	7.9
35	10	432.8	15.5	99663	7.8
40	10	447.9	15.9	102758	7.9

Table 3. Principal out-comings from numerical models and derived quantities. Columns show fault dip angle, convergence rate, differential stress at BDT, BDT depth, calculated seismogenic volume and potential magnitude derived from seismogenic volume.